Revival resonant scattering, perfect caustics and isotropic transport of pseudospin-1 particles

Hong-Ya Xu[1] and Ying-Cheng Lai[1,2,*]

[1]*School of Electrical, Computer and Energy Engineering, Arizona State University, Tempe, Arizona 85287, USA*

[2]*Department of Physics, Arizona State University, Tempe, Arizona 85287, USA*

(Dated: July 22, 2016)

Abstract

We report drastically new physics associated with wave scattering in pseudospin-1 systems whose band structure consists of a conventional Dirac cone and a topologically flat band. First, for small scatterer size, we find a surprising revival resonant scattering phenomenon and identify a peculiar type of boundary trapping profile through the formation of unusual fusiform vortices as the physical mechanism. Second, for larger scatterer size, a perfect caustic phenomenon arises as a manifestation of the super-Klein tunneling effect, leading to the scatterer's being effectively as a Vaselago lens. Third, in the far scattering field, an unexpected isotropic behavior emerges at low energies, which can be attributed to the vanishing Berry phase for massless pseudospin-1 particles and, consequently, to constructive interference between the time-reversed backscattering paths. We develop an analytic theory based on the generalized Dirac-Weyl equation to fully explain these phenomena and articulate experimental schemes with photonic or electronic systems.

PACS numbers: 03.65.Nk,03.65.Pm,03.65.Vf,03.65.Sq

* Ying-Cheng.Lai@asu.edu

I. INTRODUCTION

Solid state materials whose energy bands contain a Dirac cone structure have been an active area of research since the experimental realization of graphene [1, 2]. From the standpoint of quantum transport, the Dirac cone structure and the resulting pseudospin characteristic of the underlying quasiparticles can lead to unconventional physical properties/phenomena such as high carrier mobility, anti-localization, chiral tunneling, and negative refractive index, which are not usually seen in traditional semiconductor materials. Moreover, due to the underlying physics being effectively governed by the Dirac equation, relativistic quantum phenomena such as Klein tunneling, Zitterbewegung, and pair creations can potentially occur in solid state devices and be exploited for significantly improving or even revolutionizing conventional electronics. Uncovering/developing alternative materials with a Dirac cone structure has also been extremely active [3, 4]. In this regard, the discovery of topological insulators [5, 6] indicates that Dirac cones with a topological origin can be created, leading to the possibility of engineering materials to generate remarkable physical phenomena such as zero-field half-integer quantum Hall effect [7], topological magneto-electric effect [8], and topologically protected wave transport [9, 10].

A parallel line of research has focused on developing photonic materials with a Dirac cone structure, due to the natural analogy between electromagnetic and matter waves. For example, photonic graphene [11, 12] and photonic topological insulators [13–18] have been realized, where novel phenomena of controlled light propagation have been demonstrated. Due to the much larger wavelength in optical materials as compared with the electronic wavelength, synthetic photonic devices with a Dirac cone structure can be fabricated at larger scales with great tunabilities through modulations. The efforts have led to systems with additional features in the energy band together with the Dirac cones, opening possibilities for uncovering new and "exotic" physics with potential applications that cannot even be conceived at the present.

The materials assumed in our work are those whose energy bands consist of a pair of Dirac cones and a topologically flat band, electronic or optical. For example, in a dielectric photonic crystal, Dirac cones can be induced through unusual accidental degeneracy that occurs at the center of the Brillouin zone. This effectively makes the crystal a zero-refractive-index metamaterial at the unusual Dirac point where the Dirac cones intersect with another flat band [19–23]. Alternatively, configuring an array of evanescently coupled optical waveguides into a Lieb lattice [24–27] can lead to a gapless spectrum consisting of a pair of common Dirac cones and a perfectly flat middle band at the corner of the Brillouin zone. As demonstrated more recently, loading cold atoms into an optical Lieb lattice provides another experimental realization of the gapless three-band spectrum at a smaller scale with greater dynamical controllability of the system parameters [28]. With respect to creating materials whose energy bands consist of a pair of Dirac cones and a topologically flat band, there have also been theoretical proposals on Dice or $\mathcal{T}_3$ optical lattices [29–34] and electronic materials such as transition-metal oxide $SrTiO_3/SrIrO_3/SrTiO_3$ trilayer heterostructures [35], 2D carbon or MoS_2 allotropes with a square symmetry [36, 37], $SrCu_2(BO_3)_2$ [38] and graphene-In_2Te_2 bilayer [39].

In spite of the diversity and the broad scales to realize the band structure that consists of two conical bands and a characteristic flat band intersecting at a single point in

different physical systems, there is a unified underlying theoretical framework: a generalized Dirac-Weyl equation for massless spin-1 particles [31]. For convenience, we call such systems pseudospin-1 Dirac cone systems. Comparing with the conventional Dirac cone systems with massless pseudospin/spin-1/2 quasiparticles (i.e., systems without a flat band), pseudospin-1 systems can exhibit quite unusual physics such as super-Klein tunneling for the two conical (linear dispersive) bands [23, 32, 40, 41], diffraction-free wave propagation and novel conical diffraction [24–27], flat band rendering divergent dc conductivity with a tunable short-range disorder [42], unconventional Anderson localization [43, 44], flat band ferromagnetism [28, 45, 46], and peculiar topological phases under external gauge fields or spin-orbit coupling [35, 47–49]. Especially, the topological phases arise due to the flat band that permits a number of degenerate localized states with a topological origin (i.e., "caging" of carriers) [50]. Most existing works, however, focused on the physics induced by the additional flat band, and the scattering/transport dynamics in pseudospin-1 systems remains largely unknown (except the super-Klein tunneling behavior). Our main question is the following: what types of transport properties can arise form pseudospin-1 systems whose band structure is characterized by coexistence of a pair of Dirac cones and a flat band? To address this question in the simplest possible setting while retaining the essential physics, we study ballistic wave scattering against a circularly symmetric potential barrier. We note that for conventional Dirac cone systems with pseudospin or spin-1/2 quasiparticles, there has been extensive work on scattering [51–53] with phenomena such as caustics [54], Mie scattering resonance [55], birefringent lens [56], cloaking [57], spin-orbit interaction induced isotropic transport and skew scattering [58, 59], and electron whispering gallery modes [60]. To our best knowledge, prior to our work there were no corresponding studies for pseudospin-1 Dirac cone systems.

Our main findings are three: revival resonant scattering, super-Klein tunneling induced perfect caustics, and universal low-energy isotropic transport without broken symmetries for massless quasiparticles. First, for small scatterer size, the effective three-component spinor wave exhibits revival resonant scattering as the incident wave energy is varied continuously - a phenomenon that has not been reported in any known wave systems. Strikingly, the underlying revival resonant modes show a peculiar type of boundary trapping profile in their intensity distribution. While the profile resembles that of a whispering gallery mode, the underlying mechanism is quite different: these modes occur in the wave dominant regime through the formation of unusual fusiform vortices around the boundary in the corresponding local current patterns, rather than being supported by the gallery type of orbits through total internal reflections. Second, for larger scatterer size so that the scattering dynamics is in the semiclassical regime, a perfect caustic phenomenon arises when the incident wave energy is about half of the barrier height, as a result of the super-Klein tunneling effect. A consequence is that the scatterer behaves as a lossless Vaselago lens with effective negative refractive index resulting from the Dirac cone band structure. Compared with conventional Dirac cone systems for pseudospin-1/2 particles, the new caustics possess remarkable features such as significantly enhanced focusing, vanishing of the second and higher order caustics, and a well-defined static cusp. Third, in the far scattering field, an unexpected isotropic behavior arises at low energies. Considering that there is no broken symmetry so the quasiparticles remain massless, the phenomenon is quite surprising as conventional wisdom suggests that the scattering be anisotropic. In particular, by analyzing the characteristic ratio of the

transport to the elastic time as a function of the scatterer size, we find that the phenomenon of scattering isotropy can be attributed to the vanishing of the Berry phase for massless pseudospin-1 particles that results in constructive interference between the time-reversed backscattering paths. Because of the isotropic structure, the emergence of a Fano-type resonance structure in the function of the ratio versus the scatterer size can be exploited to realize an effective switch of the wave propagation from a forward dominant state to a backward dominant one, and vice versa. We develop an analytic theory with physical reasoning to understand the three novel phenomena, and articulate experimental verification schemes with photonic or electronic systems.

II. RESULTS

We consider scattering of pseudospin-1 particle from a circularly symmetric scalar potential barrier of height V_0 defined by $V(r) = V_0\Theta(R-r)$, where R is the scatterer radius and Θ denotes the Heaviside function. The band structure for the particle consists of a pair of Dirac cones and a flat band. A comprehensive description of the Hamiltonian, its properties, the boundary conditions, and detailed solutions of the scattering waves is given in **Supplementary Materials**. To characterize the scattering dynamics quantitatively, we use the scattering efficiency, defined as a ratio of the scattering to the geometric cross sections [55]:

$$Q = \frac{\sigma}{2R}, \tag{1}$$

where the scattering cross section σ can be calculated through the far field radial reflected current, as detailed in **Supplementary Materials**.

A. Near-field behavior 1: Revival resonant scattering

To uncover unusual physics, we calculate and analyze the scattering efficiency Q as a function of the reduced barrier strength V_0R and the relative incident energy E/V_0. In order to highlight the unique manifestations of the unconventional band structure, we focus on the under barrier scattering process in which the particle energy is below the barrier height: $0 < E/V_0 < 1$. To be concrete, we choose $E/V_0 = 0.01, 0.1, 0.9$ and, for each fixed value of E/V_0, we calculate the scattering efficiency Q versus the barrier strength V_0R. For the three chosen values of E/V_0, the results are shown by the respective red curves in Figs. 1(a-c). We see that there are well-separated sharp resonances in Q for small values of E/V_0 [e.g., Fig. 1(a)], while broadened and overlapping ripple structures occur for larger values of E/V_0 [e.g., Figs. 1(b) and 1(c)]. Using the characteristic size parameter kR, we can generally classify two distinct scattering regimes: $kR \ll 1$ and $kR \gg 1$. In the former case ($kR \ll 1$), the incident wavelength $2\pi/k$ is much larger than the range R of the scattering potential. In this case, the wave effects dominate the scattering behavior with a remarkable resonance characteristic, as shown in Figs. 1(a) and 1(b). The case $kR \gg 1$ corresponds to the semiclassical limit where the classical ray picture is applicable. In this case, the scatterer acts essentially as a Veselago reflector/lens due to an equivalent negative refractive index arising from the particular band structure of Dirac cones and a flat band.

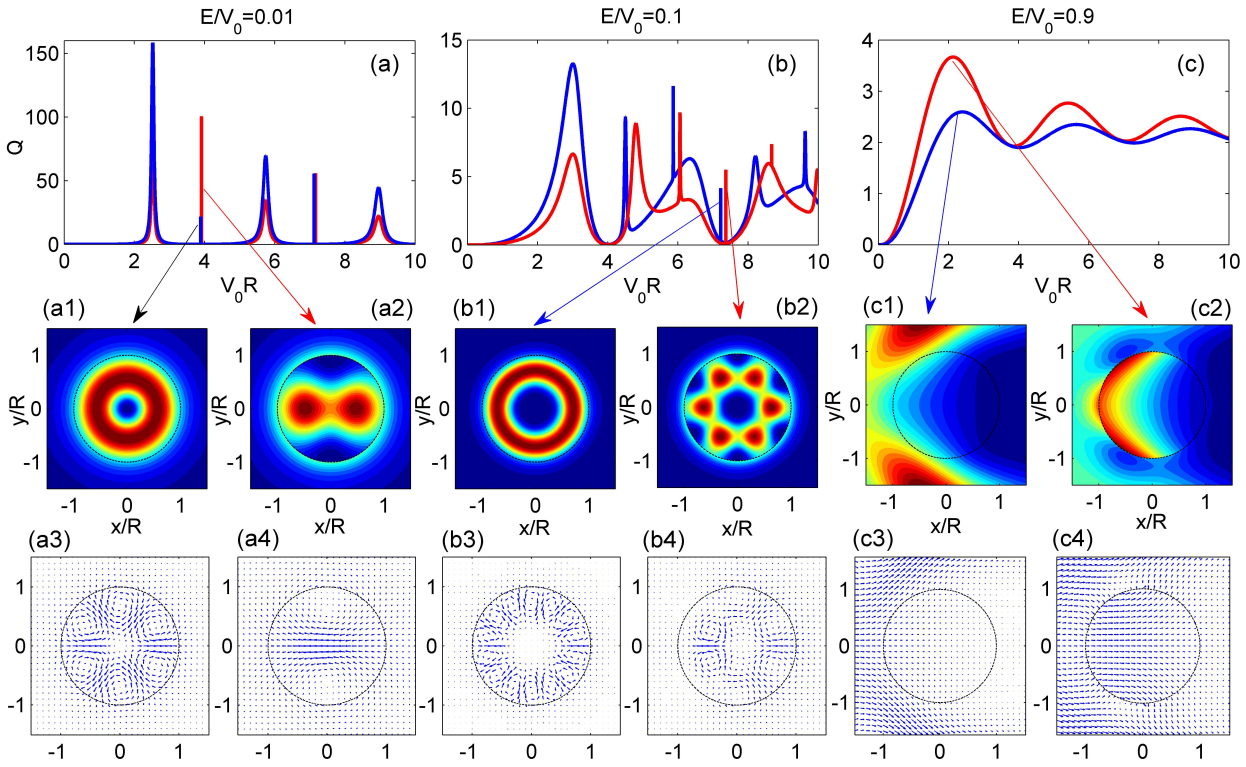

FIG. 1: General behaviors of the scattering efficiency versus the scatterer strength. Scattering efficiency Q as a function of the scatterer strength V_0R for a number of values of the relative incident energy: (a) $E/V_0 = 0.01$, (b) $E/V_0 = 0.1$, and (c) $E/V_0 = 0.9$. The middle and bottom panels show the corresponding probability density and local current density profiles, respectively. In (a-c), the blue curves are for the conventional massless pseudospin/spin-1/2 case while the red ones are for the massless pseudospin-1 wave system.

From the explicit summation form of Q and the reflection coefficients A_l (labeled by the angular momentum l) obtained within the generalized partial-wave decomposition formalism in **Supplementary Materials**, we see that the size parameter kR provides a general estimate of the maximum number of angular momentum channels contributing to the scattering process. Accordingly, we can obtain a closed form of Q in the limit of $kR \ll 1$, where only a few lowest channels dominate for a given range of the barrier strength, say $V_0R \in [0.01, 10]$. Specifically, using the short-range ($x \ll 1$) behavior of the Bessel functions appearing in the solutions of the scattering problem, we get a closed expression for the dependence of the scattering efficiency Q on the effective barrier strength V_0R for $kR \ll 1$ and $E/V_0 \ll 1$, which reads

$$Q \approx \frac{2}{kR}\left[\frac{\Gamma_0^2}{\Gamma_0^2 + \left(V_0R - x_0 + kR\ln\left(\gamma_E kR/2\right)\right)^2} + 2\times\frac{\Gamma_1^2}{\Gamma_1^2 + \left(V_0R - x_1 - kR\right)^2}\right], \qquad (2)$$

where γ_E is the constant appearing in the small value approximation of the Bessel function: $Y_0(x) \approx (2/\pi)\ln(\gamma_E x/2)$for $x \ll 1$ and the lowest $|l| = 0, 1$ channels give the leading contribution to and hence dominate the scattering process with well-separated symmetric sharp resonances around $V_0R = x_0, x_1$ that correspond to the zeros of the Bessel functions

J_0 and J_1. The respective lifetimes are given by

$$\frac{1}{\Gamma_0} = \frac{2}{\pi kR} \quad \text{and} \quad \frac{1}{\Gamma_1} = \frac{2}{\pi (kR)^3}.$$

From Eq. (2), we see that, for $kR \ll 1$ and $E/V_0 \ll 1$, the resonances exhibit a Lorentzian shape (also known as the Breit-Wigner distribution). Due to their longer lifetime: $1/\Gamma_1 \gg 1/\Gamma_0$, the resonances associated with the $|l| = 1$ channel are much narrower than those with $l = 0$. In the limit $kR \to 0$, the resonant excitations are typically positioned at the zeros of $J_l(V_0R)$ with an infinite lifetime (i.e., zero resonant widths) that physically correspond to a bound state in the antidot potential profile without an incident wave. Further insights can be gained by considering the local probability and current density distributions of one particular excitation of the normal modes, e.g., the first resonance associated with the $|l| = 1$ channel, as indicated in Figs. 1(a2) and 1(a4). Analytically, we obtain the probability density inside the scattering region ($r < R$) as

$$\rho_< \approx |B_1|^2 \left[J_1^2(V_0 r) + \frac{J_0^2(V_0 r) + J_2^2(V_0 r)}{2} + \left(J_1^2 - J_0 J_2 \right) \cos(2\theta) \right], \tag{3}$$

together with the local current distribution

$$\begin{aligned} \boldsymbol{j}_< \approx & - \Re(B_1^* B_0) \left[2J_1^2(V_0 r) + J_0^2(V_0 r) - J_0(V_0 r) J_2(V_0 r) \right] \cos\theta \hat{e}_r \\ & + \Re(B_1^* B_0) J_0(V_0 r) \left[J_0(V_0 r) + J_2(V_0 r) \right] \sin\theta \hat{e}_\theta, \end{aligned} \tag{4}$$

where $\Re(B_1^* B_0)$ denotes the real part of $(B_1^* B_0)$, and B_l are the transmission coefficients (**Supplementary Materials**). When a scattering resonance emerges, the magnitude of the transmission coefficient behaves as

$$|B_1| \sim \frac{1}{kRJ_1(V_0R)} \gg 1,$$

leading to a noticeable probability density concentration inside the scatterer, indicating the occurrence of wave trapping/confinement. Moreover, it follows from Eq. (4) that, accompanying the confinement, a vortex pattern symmetric with respect to the $x-$axis is formed. In general, in the resonant scattering regime, the incident wave is confined/trapped in vortices (as demonstrated in the bottom panel of Fig. 1) rather than through the conventional total internal reflection mechanism.

Comparing with the conventional pseudospin-1/2 Dirac cone systems [cf., Figs. 1(a1) and 1(a3), as well as the blue curve in Fig. 1(a)], we see that there are common features in the scattering curve and trapping mechanism but with different resonant wave/current patterns. In particular, the trapping intensity distribution is radially symmetric for the pseudospin-1/2 case, but for a pseudospin-1 particle, there is an angular dependence of the scattering amplitude with a well-defined rotational symmetry, which can be analyzed for a specific resonant mode using Eq. (3).

Given the particular range of the scattering strength V_0R as set in Figs. 1(a-c), we see that increasing E/V_0 leads to larger values of kR and hence the scattering process involves higher angular momentum channels. As a result, more quasi-bound modes can be excited, generating overlapping and broadened resonances, as shown in Figs. 1(b) and 1(c). In the

limit of $kR \gg 1$, say $V_0R \gg 1$ for $E/V_0 \sim 1$, we enter the semiclassical regime where the ray picture is applicable. We obtain $Q \approx 2\,[1 - \pi\cos(2V_0R - \pi/4)/4V_0R]$ as a damped oscillatory function of the scattering strength V_0R about a constant value, as shown in Fig. 1(c). Distinct from the resonant scattering regime dominated by wave interference/diffraction, in the semiclassical regime the scatterer acts as a Veselago reflector due to its effective negative refractive index. The associated local probability density and current density patterns in typical situations for both the conventional massless pseudospin-1/2 and the massless pseudospin-1 cases are shown in Figs. 1(b1-b4) and 1(c1)-(c4), respectively.

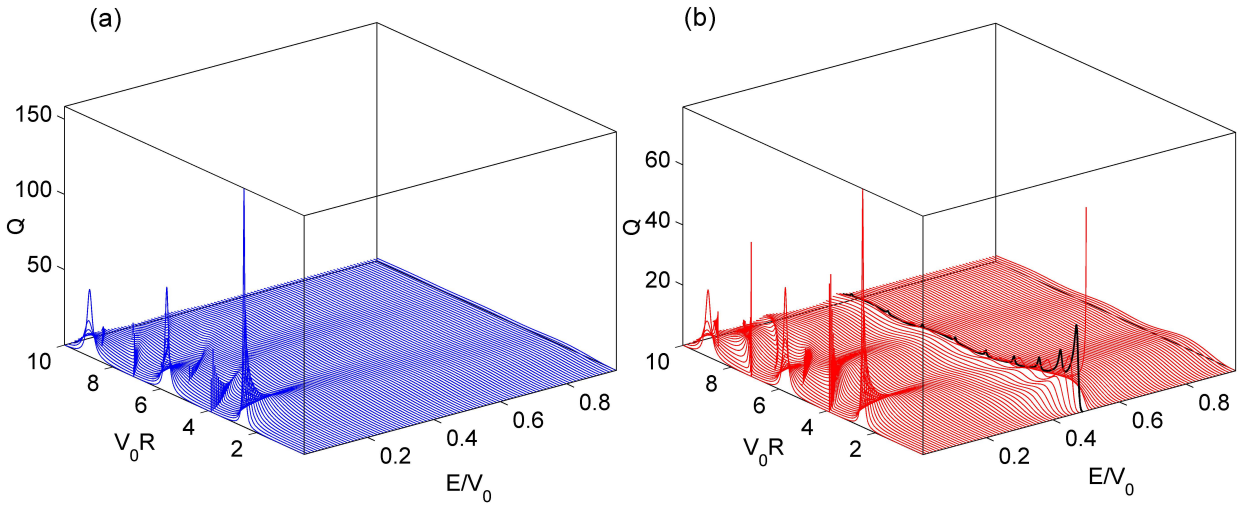

FIG. 2: Scattering efficient Q versus the scatterer strength V_0R and the relative incident energy E/V_0 for (a) massless pseudospin-1/2 and (b) massless pseudospin-1 wave systems.

To gain further insights into the scattering behaviors, we plot Q as a function of V_0R and E/V_0, as shown in Figs. 2(a) and 2(b). As expected, for the pseudospin-1/2 Dirac cone system, the curve of Q versus V_0R tends to be smooth as E/V_0 is increased [Fig. 2(a)]. However, for the pseudospin-1 Dirac cone system shown in Fig. 2(b), the remarkable phenomenon of revival resonant scattering emerges: the sharp resonances disappear, reappear unexpectedly, and then disappear again with continuous increase in E/V_0. We emphasize that this revival phenomenon is quite exceptional which, to our knowledge, has not been reported in any other known wave systems. In the limit of $V_0R \ll 1$ ($V_0R > kR$), we obtain

$$Q \simeq \frac{2}{kR}\left[\frac{P_0^2}{P_0^2+Q_0^2} + 2\times\frac{P_1^2}{P_1^2+(4+Q_1)^2}\right], \tag{5}$$

where

$$P_0 = \pi kR, \quad \text{and}$$
$$Q_0 = 2\,[kR\ln(\gamma_E kR/2) - J_0(V_0R-kR)/J_1(V_0R-kR)]\,,$$

with P_1 and Q_1 given by $[P_1, Q_1] = kR[P_0, Q_0]$. The first term of Eq. (5),

$$\frac{P_0^2}{P_0^2+Q_0^2} \approx \frac{\pi^2 J_1^2(V_0R-kR)}{4J_0^2(V_0R-kR)}(kR)^2 \simeq \frac{\pi^2(1-E/V_0)^2}{16}(V_0R)^2(kR)^2 \ll 1,$$

is off-resonance. Remarkably, the second term generates an additional resonance for $4+Q_1 = 0$, which corresponds to the emerging revival resonance observed. Explicitly, the associated revival resonant condition can be obtained from $4 + kRQ_0 = 0$ as $E/V_0 \approx 1/2$, which agrees with the numerical results as displayed in Fig. 2(b).

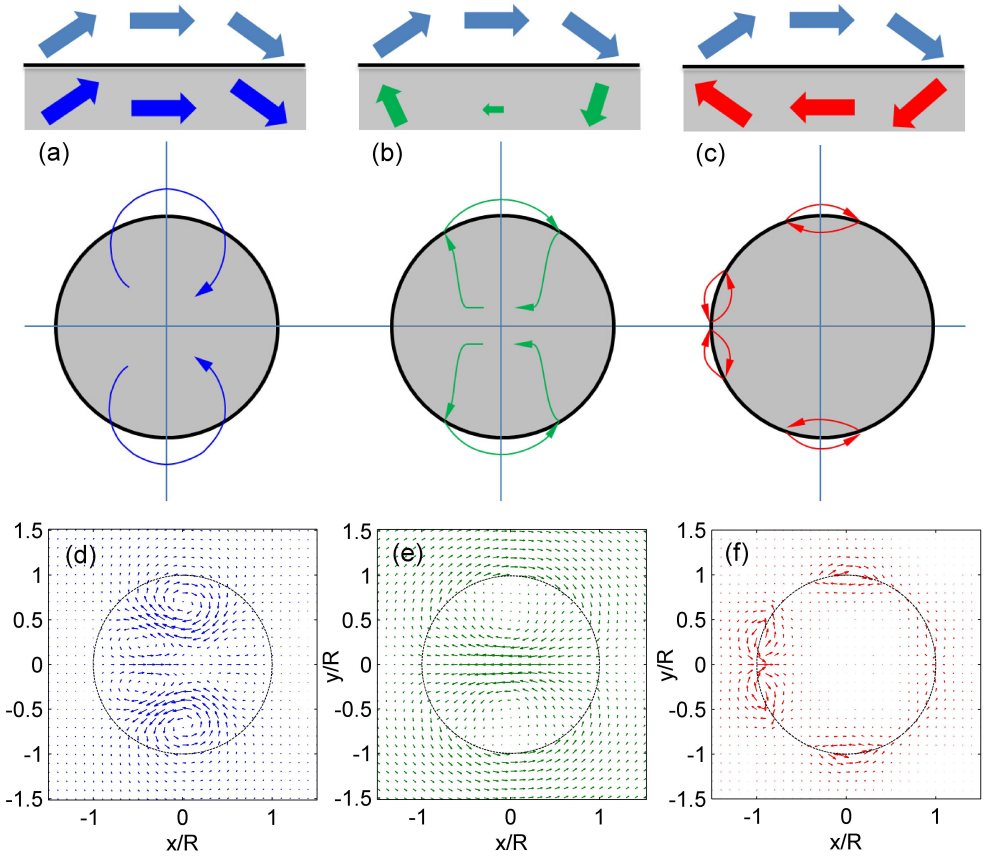

FIG. 3: Vortex-based wave trapping for massless pseudospin-1 scattering. (a-c) Schematic illustration of three types of vortex-based wave trapping. (d) Wave pattern near the boundary for a massless pseudospin-1/2 particle for $E/V_0 = 0.086$. (e,f) Boundary wave patterns for the massless pseudospin-1 case for $E/V_0 = 0.044$ and $E/V_0 = 0.487$, respectively. The value of V_0R is set to be 4.5 for all cases.

Certain remarkable features of the revival resonances can be revealed through the underlying revival resonant modes (RRMs) defined in terms of the associated local probability and current density patterns. We find that the RRMs exhibit unusual boundary trapping profiles, where the higher the resonance frequency (energy) the more pronounced the trapping. Examining the corresponding local current density distribution of a specific RRM, we find that the incident wave is fed into fusiform vortices about the boundary and is trapped there. In contrast, for conventional pseudospin-1/2 scattering, no such trapping phenomenon occurs. Using the general vortex-based trapping mechanism, we can get an intuitive physical picture for the unusual boundary trapping phenomenon through a qualitative analysis of vortex formation in the local current distribution stipulated by the boundary conditions. In particular, for a given local current configuration outside the scattering boundary, as

indicated by the light blue arrows in Figs. 3(a-c), we sketch the possible local current patterns inside the boundary, denoted by the blue, green and red arrows, respectively. This can be done with the boundary conditions defined in terms of the spinor wavefunction $\Psi = [\psi_1, \psi_2, \psi_3]^T$ and their effect on the associated local current field $\boldsymbol{j}$ (see **Supplementary Materials**). Since continuity is the only constraint on the normal component of the local currents at the boundary (the tangent component is in general discontinuous and can even have opposite directions), there is an additional freedom to configure the corresponding current pattern inside the potential region for a particular pattern outside. This leads to the remarkable fusiform boundary vortices as illustrated in Fig. 3(c) with the dramatic phenomenon of boundary trapping and, consequently, to the resonances in the curve of the scattering efficiency. Note that, for the conventional scalar or spinor wave systems, the current configuration is well-determined in the sense that, given a configuration on one side of the boundary, that on the other side is then determined completely. This is due to the continuity in both components of the local currents at the boundary, as illustrated in Fig. 3(a). As a concrete example, we demonstrate the full local current patterns as in Figs. 3(d-f), where the former two represent the typical local current profiles underlying the conventional low-order resonant modes excited in the massless pseudospin-1/2 and massless pseudospin-1 wave systems, respectively, while the last one is for that of the RRM that arises only for the massless pseudospin-1 wave system.

For pseudospin-1 Dirac cone systems, a remarkable phenomenon is super-Klein tunneling (see **Supplementary Materials**), which occurs when the energy of the incident particle is about one half of the potential height. In this case, forward scattering is maximized. In contrast, the revival scattering resonances are associated with fusiform vortices about the boundary, creating perfect wave trappings there and eliminating any forward scattering. Both super-Klein tunneling and revival resonant scattering depend on the scatterer strength V_0R and the relative incident energy E/V_0. From an applied point of view, it is thus possible to switch the super-Klein-tunneling dominant forward scattering on and off efficiently by tuning the parameters. In fact, the higher pseudospin degree of freedom and the flexible scattering boundary conditions render richer current patterns that can be manipulated through parameter perturbation. This may find applications in novel photonic integrated circuit design, as pseudospin-1 systems have been realized experimentally in a variety of photonic crystals [19, 20, 23–26, 28].

While the RRMs uncovered appear similar to the well-known whispering gallery modes (WGMs) in terms of the intensity profiles, we emphasize that the underlying mechanisms are quite different. In particular, the WGMs are due to the total internal reflection within an effective semiclassical ray regime, but the RRMs result from the formation of unusual, dominant vortices locally attached to the boundary due to wave interference and can thus occur for much smaller scatterer size kR, a regime in which the semiclassical ray approximation fails.

B. Near-field behavior 2: perfect caustics

Caustics, a spatial region in which the density of light rays is singular, occurs in the semiclassical regime. This phenomenon is quite common in daily life, mostly through geometric optics. For a pseudospin-1/2 Dirac cone system, caustics can occur due to the tunable effec-

tive negative refractive index and the Klein tunneling effect, as shown in Figs. 4(a) and 4(c). For the pseudospin-1 Dirac cone system, the surprising phenomenon of perfect caustic/lens behavior occurs, as shown in Figs. 4(b) and 4(d) for the same parameter as in Figs. 4(a) and 4(c), which emerges in the regime where the incident wavelength is much smaller than the scatterer radius R. The caustic patterns for the massless pseudospin-1 system are "perfect" in the sense that they are significantly more focused/concentrated than the pseudospin-1/2 counterparts. We find that perfect caustics are a result of the super-Klein tunneling effect for the massless pseudospin-1 particle, where the transmission coefficient approaches unity for *any* incident angle. Specifically, for a single straight scattering interface, we obtain the transmission coefficient for incident angle θ ($1\pi/2 \leq \theta \leq \pi/2$) as

$$T = \frac{4\tau\tau' \cos\theta' \cos\theta}{\cos^2\theta' + \cos^2\theta + 2\tau\tau' \cos\theta' \cos\theta}, \tag{6}$$

with the refractive angle given by

$$\theta' = \pi - \tan^{-1} \frac{|E/V_0| \sin\theta}{\sqrt{(1 - E/V_0)^2 - (E/V_0)^2 \sin^2\theta}},$$

where $\tau = \mathrm{sgn}(E)$ and $\tau' = \mathrm{sgn}(E - V_0)$. It follows from Eq. (6) that $T \equiv 1$ for $E/V_0 = 1/2$, regardless of the incident angle, as shown by the thick red curve in Fig. 5, signifying a super-Klein tunneling behavior. For comparison, the incident angle dependent transmission probability for the conventional pseudospin-1/2 system is shown as the thick blue line in the same figure.

Within the ray formalism and based on differential geometry [54], we obtain analytically the following caustic envelope equation defining a curve $\boldsymbol{r}_c = (x_c, y_c)$ as

$$\frac{\boldsymbol{r}_c(p,\theta)}{R} = (-)^{p-1} \left[(-\cos\Theta, \sin\Theta) + \cos\beta \frac{1 + 2(p-1)\beta'}{1 + (2p-1)\beta'} \times (\cos(\Theta + \beta), -\sin(\Theta + \beta)) \right], \tag{7}$$

where $\Theta = \theta + 2(p-1)\beta$, $\sin\beta = \sin\theta/|1 - V_0/E|$, and $\beta' = \cos\theta/\sqrt{(1 - V_0/E)^2 - \sin^2\theta}$ with p being the number of chords inside the scattering region corresponding to $p-1$ internal reflections. Intuitively, the caustics for $p > 1$ are less visible since the ray intensity decreases after each internal reflection. However, for our pseudospin-1 Dirac cone system, the super-Klein tunneling effect for $E/V_0 = 1/2$ will suppress the $p > 1$ caustics completely, leading to a perfect caustic for $p = 1$, which intuitively can be better seen from the corresponding local current patterns in Figs. 4(c,d).

C. Far-field behavior: isotropic scattering of massless pseudospin-1 quasiparticles and control

Far away from the scattering center, i.e., $r \gg R$, for unit incident density, the spinor wavefunction can be written as

$$\Psi_>(r,\theta) \approx \frac{1}{2} \begin{pmatrix} 1 \\ \sqrt{2}\tau \\ 1 \end{pmatrix} e^{ikr\cos\theta} + \frac{1}{2} \begin{pmatrix} e^{-i\theta} \\ \sqrt{2}\tau \\ e^{i\theta} \end{pmatrix} \frac{f(\theta)}{\sqrt{r}} e^{ikr}, \tag{8}$$

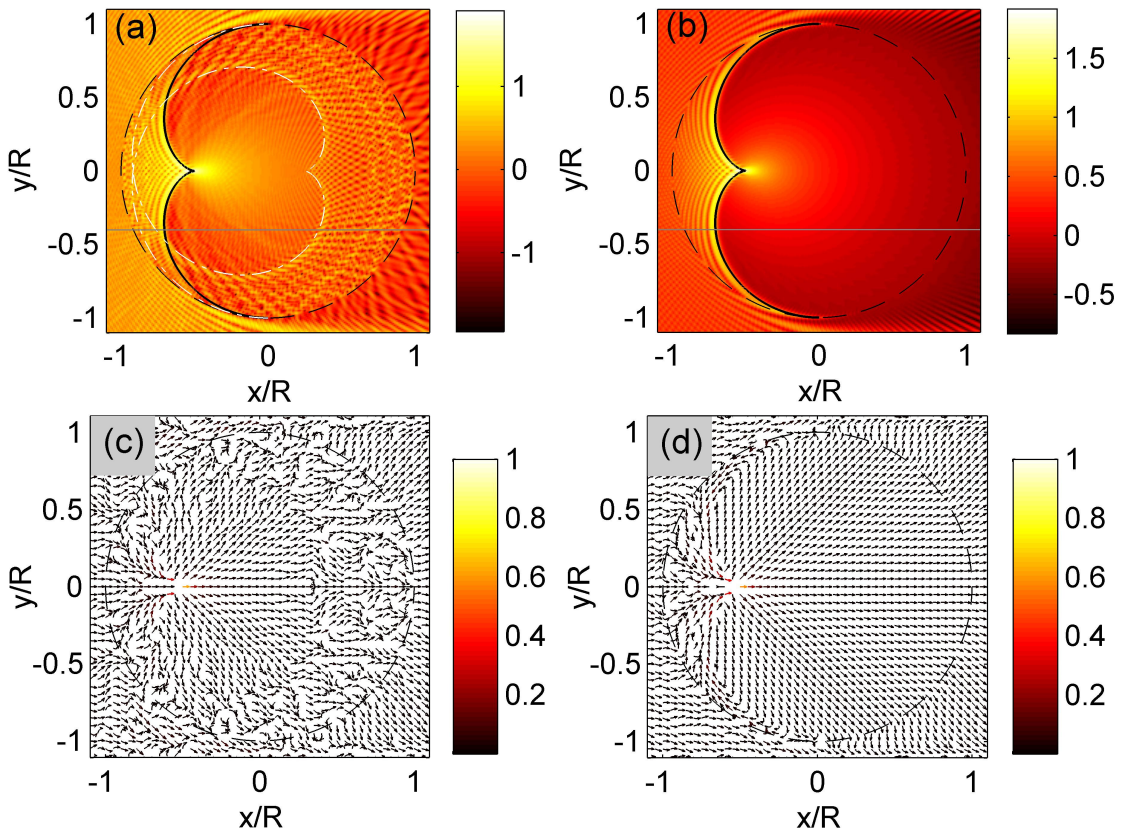

FIG. 4: Caustic behavior in the semiclassical regime and perfect caustics in pseudospin-1 Dirac cone systems. The probability and local current density patterns, respectively, for (a,c) conventional pseudo-1/2 and (b,d) pseudospin-1 Dirac cone systems. The probability density patterns in (a) and (b) are plotted on a logarithmic scale. The corresponding local current density patterns in (c) and (d) are color-coded with magnitude normalized by its maximum. The parameters are $R = 300$ and $E/V_0 = 1/2$.

where $f(\theta)$ denotes the 2D far-field scattering amplitude in the direction defined by the angle θ with the x axis. The differential and the total cross sections are given, respectively, by

$$\frac{\mathrm{d}\sigma}{\mathrm{d}\theta} = \tau |f(\theta)|^2, \tag{9}$$

and

$$\sigma = \tau \int_0^{2\pi} |f(\theta)|^2 \mathrm{d}\theta. \tag{10}$$

In addition, we define the transport or momentum-relaxation cross section as

$$\sigma_{\mathrm{tr}} = \tau \int_0^{2\pi} \mathrm{d}\theta |f(\theta)|^2 (1 - \cos\theta). \tag{11}$$

The three types of cross sections are experimentally measurable and can be used to quantitatively characterize the basic scattering and transport physics for pseudospin-1 Dirac cone

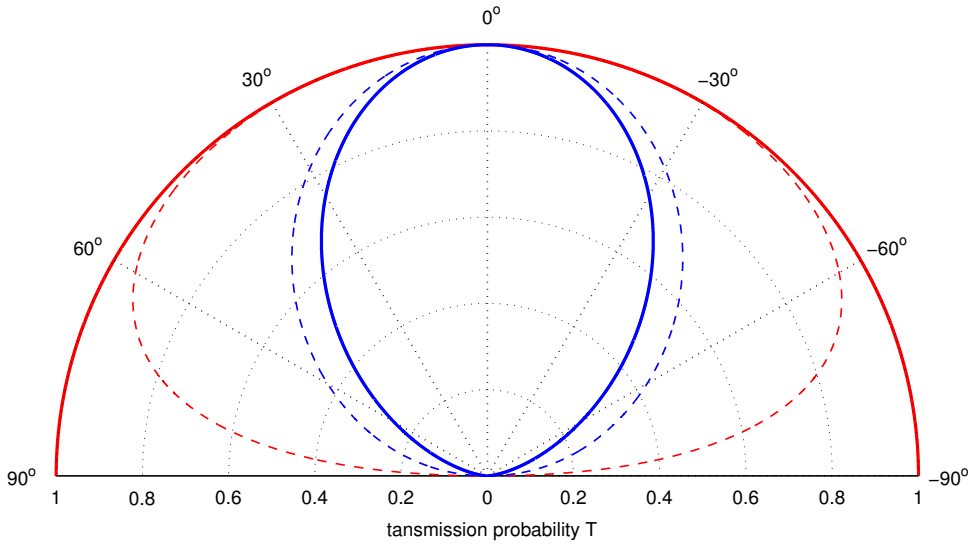

FIG. 5: Super-Klein tunneling in pseudospin-1 Dirac cone systems. Transmission probability: red and blue curves are for the massless pseudospin-1 and pseudospin-1/2 particles, respectively, with $E/V_0 = 0.5$ (solid lines) and $E/V_0 = 0.4$ (dash lines). For the former (solid red line) the transmission is unity, regardless of the incident angle.

systems. For example, consider such a system with randomly distributed identical scatterers of low concentration, i.e., $n_c \ll 1/R^2$, the conductivity in units of the conductance quantum G_0 can be expressed as

$$\frac{G}{G_0} = \frac{k}{n_c \sigma_{\rm tr}} = v_g k \tau_{\rm tr}, \tag{12}$$

where the sample size is assumed to be larger than the mean-free path $L = v_g \tau_{\rm tr}$ with $\tau_{\rm tr}$ being the transport mean free time, and v_g is the group velocity. The elastic scattering time (the quantum lifetime) τ_e can be determined from the total cross section through

$$\frac{1}{\tau_e} = n_c v_g \sigma. \tag{13}$$

The two time scales defines the following characteristic ratio:

$$\xi = \frac{\tau_{\rm tr}}{\tau_e} = \frac{\sigma}{\sigma_{\rm tr}} \equiv \frac{\oint {\rm d}\theta |f(\theta)|^2}{\oint {\rm d}\theta |f(\theta)|^2 (1 - \cos\theta)}, \tag{14}$$

which can be used to characterize the far-field behavior of the scattering process. Through a detailed analysis, we obtain the following formula (see **Supplementary Materials**):

$$\xi = \frac{2 \sum_l \sin^2 \delta_l}{\sum_l \sin^2(\delta_{l+1} - \delta_l)}, \tag{15}$$

where δ_l is the scattering phase shift associated with angular momentum l.

We present our finding of the general isotropic nature of low-energy scattering for massless pseudospin-1 wave. To be concrete, we calculate from Eq. (15) the ratio ξ as a function of kR for a given barrier strength $V_0 R = 5$. The result is shown as the red curves in Fig. 6,

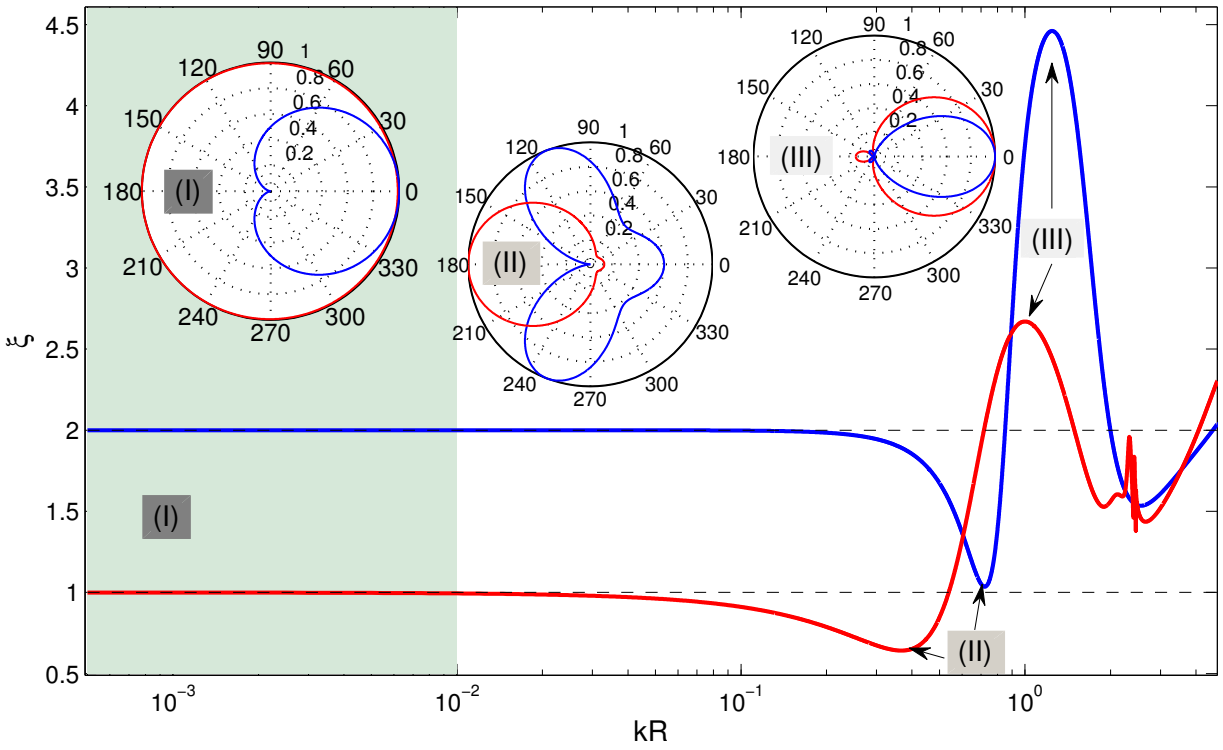

FIG. 6: Isotropic scattering of massless pseudospin-1 quasiparticle. Ratio ξ as a function of kR for $V_0R = 5$: the red and blue lines are for the massless pseudospin-1 and pseudospin-1/2 cases, respectively.

where we see that there is a characteristic constant ratio $\xi \approx 1$ of the transport time to the elastic time for $kR \ll 1$. For comparison, we calculate the corresponding ratio for the massless pseudospin-1/2 wave, where low-energy scattering is universally anisotropic as characterized by a constant ratio $\xi \approx 2$ [53, 58]. Our result indicates that, for massless pseudospin-1 particles back scattering is as pronounced as forward scattering. This finding is quite counterintuitive as, if the massless nature of the quasiparticles is sustained, they can penetrate through potential barriers of arbitrary strength via the mechanism of Klein tunneling, making forward scattering more pronounced. While super-Klein tunneling can occur for massless pseudospin-1 quasiparticles, the scattering in the system is isotropic at low energies. This means that, to generate isotropic transport, it may not be necessary to break symmetries to alter the massless nature of the quasiparticles through, e.g., additional mechanisms such as spin-orbit interactions. Equivalently, an isotropic ratio ξ for massless quasiparticles does not necessarily imply any symmetry breaking leading to a finite mass.

To gain deeper insights into the physics underlying the counterintuitive phenomenon of isotropic scattering for massless particles, we analyze the characteristic ratio ξ in terms of the scattering cross sections. The reflection coefficient associated with angular momentum l satisfies $A_l = A_{-l}$. Using this relation, we obtain the differential cross section as

(**Supplementary Materials**)

$$\frac{\mathrm{d}\sigma}{\mathrm{d}\theta} = \frac{2\tau}{\pi k}\{|A_0|^2 + 2\sum_{n=1}^{\infty}|A_n|^2[1+\cos(2n\theta)] + 4\sum_{n=1}^{\infty}\Re(A_0A_n^*)\cos(n\theta) \\ + 8\sum_{m>n=1}^{\infty}\Re(A_nA_m^*)\cos(n\theta)\cos(m\theta)\}. \tag{16}$$

In the regime $kR \ll 1$ where the total angular momentum channels ($l = 0, \pm 1$) dominate the scattering process, we have

$$\frac{\mathrm{d}\sigma}{\mathrm{d}\theta} \approx \frac{2\tau}{\pi k}\left\{|A_0|^2 + 2|A_1|^2[1+\cos(2\theta)]\right\}, \tag{17}$$

resulting in an isotropic ratio that agrees with the simulation result:

$$\xi \equiv \frac{\oint \mathrm{d}\theta \frac{d\sigma}{d\theta}}{\oint \mathrm{d}\theta \frac{d\sigma}{d\theta}(1-\cos\theta)} \approx 1. \tag{18}$$

A remarkable feature associated with the expression of $\mathrm{d}\sigma/\mathrm{d}\theta$ in Eq. (17) is the presence of backscattering characterized by a finite differential cross section at $\theta = \pi$:

$$\frac{\mathrm{d}\sigma}{\mathrm{d}\theta}\Big|_{\theta=\pi} = \frac{2\tau}{\pi k}\left[|A_0|^2 + 4|A_1|^2\right], \tag{19}$$

which results from the constant term contributed by the $l = 0$ channel and the constructive interference between the time-reversed scattering paths denoted by $l = \pm 1$. The underlying physical picture can then be understood, as follows. Consider the pseudohelicity defined as $\hat{h} = \boldsymbol{S}\cdot\boldsymbol{k}/k$. Its eigenvalues are conserved during the scattering process because of the commutation $[\hat{h}, \hat{H}] = 0$ in the massless pseudospin-1 system. In general, when the time-reversal symmetry is taken into account, a typical backscattering process consists of a pair scattering paths with a 2π relative rotation of the pseudospin between them. This leads to a phase difference determined by the underlying Berry phase $e^{i\Phi_B}$. For a massless pseudospin-1 particle, we have $\Phi_B = 0$. There is thus coherent interference for backscattering, which makes the low-energy scattering isotropic. When this general picture is applied to a conventional pseudospin-1/2 Dirac cone system with $\Phi_B = \pi$, it is straightforward to see that, for backscattering there is complete destructive interference and the zero total angular momentum channel is absent. In particular, we have, for the differential cross section, $\mathrm{d}\sigma/\mathrm{d}\theta \sim (1+\cos\theta)$ for $kR \ll 1$. The ratio ξ thus becomes $\xi \approx 2/\oint \mathrm{d}\theta(1-\cos 2\theta) = 2$. The analysis agrees with the numerical results in Fig. 6.

Another remarkable phenomenon is the emergence of Fano-like resonance profile for larger values of kR where higher angular momentum channels can be excited and interfere with the lower ones, as manifested in the behavior of ξ versus kR. This provides a way to manipulate the Klein-tunneling based scattering. In particular, for the conventional pseudospin-1/2 Dirac cone system (as illustrated by the blue curves in the insets (II) and (III) of Fig. 6), the preferred scattering directions can be controlled through tuning of the quantity kR. However, for such particles, since backscattering is typically totally suppressed, it is not possible to switch between forward and backward scattering. Remarkably, controlled switching in the

scattering dynamics from forward to backward and vice versa can be done for our pseudospin-1 system. There are in fact a number of controllable scattering scenarios ranging from the isotropic type ($\xi \approx 1$), the backscattering dominant type (ξ¡1), and the forward scattering dominant type ($\xi > 2$), and the switches among them can be realized by tuning the scattering parameter kR. The feasibility of controlled scattering can be seen from the red curves in the insets of Fig. 6. This capability of scattering control can have potential applications in unconventional photonic/electronic circuit design.

III. DISCUSSION

Using a general Hamiltonian for pseudospin-1 systems whose energy band structure constitutes a pair of Dirac cones and a topologically flat band, we investigate the basic problem of wave scattering from a circularly symmetric potential barrier. In spite of its simplicity, the system gives unusual and unexpected physics: revival resonant scattering, perfect caustics, and isotropic scattering for massless quasiparticles. In particular, for small scatterer size, the effective three-component spinor wave exhibits revival resonant (Mie) scattering features as the incident wave energy is varied continuously - a surprising phenomenon which, to our knowledge, has not been reported in any known wave systems. For larger scatter size rendering semiclassical the underlying scattering dynamics, a super-caustic phenomenon arises when the incident wave energy is about half of the barrier height, which is essentially a manifestation of the super-Klein tunneling effect for massless pseudospin-1 particles. Because of Klein tunneling, intuitively the wave scattering should be anisotropic due to the suppression of backward scattering, which is indeed the case for conventional pseudospin-1/2 particles. However, for a pseudospin-1 particle, the associated Berry phase can lead to constructive interference in the backward direction, leading to the counterintuitive phenomenon of isotropic scattering even for massless quasiparticles. We develop an analytic theory and physical understanding with extensive numerical support to substantiate our findings.

It is possible to conduct experimental test of the findings in this paper. For example, in a recent work [23], it was demonstrated for a class of two-dimensional dielectric photonic crystals with Dirac cones induced accidentally [19–22] that the Maxwell's equations can lead to an effective Hamiltonian description sharing the same mathematical structure as that for massless pseudospin-1 particles. Especially, the photonic analogy of the gate potential in the corresponding electronic system can be realized by manipulating the scaling properties of Maxwell's equations. Recent experimental realizations of photonic Lieb lattices consisting of evanescently coupled optical waveguides implemented through the femtosecond laser-writing technique [24–27] make them prototypical for studying the physics of pseudopsin-1 Dirac systems. With a particular design of the refractive index profile across the lattice to realize the scattering configuration, the findings in this paper can be experimentally tested. In addition, loading ultracold atoms into an optical Lieb lattice fabricated by interfering counter-propagating laser beams [28] provides another versatile platform to test our findings, where appropriate holographic masks can be used to implement the desired scattering potential barrier [32, 61]. In electronic systems, we note that the historically studied but only recently realized 2D magnetoplasmon system [62] is described by three-component linear equations with the same mathematical structure of massless pseudospin-1 particles, which can serve as a 2D electron gas system to test our results.

From an applied perspective, the phenomenon of revival resonant scattering can be a base for articulating a new class of microcavity lasers based on the principles of relativistic quantum mechanics. It may also lead to new discoveries in condensed matter physics through exploiting the phenomenon in electronic systems. The phenomenon of perfect caustics can have potential applications in optical imaging defying the diffraction limit as well as in optical cloaking.

---

[1] K. S. Novoselov, *et al.*, Electric field effect in atomically thin carbon films. *Science* **306**, 666-669 (2004).

[2] C. Berger, *et al.*, Ultrathin epitaxial graphite: 2D electron gas properties and a route toward graphene-based nanoelectronics. *J. Phys. Chem. B* **108**, 19912-19916 (2004).

[3] T. Wehling, A. Black-Schaffer, A. Balatsky, Dirac materials. *Adv. Phys.* **63**, 1-76 (2014).

[4] J. Wang, S. Deng, Z. Liu, Z. Liu, The rare two-dimensional materials with Dirac cones. *National Sci. Rev.* (2015).

[5] M. Z. Hasan, C. L. Kane, *Colloquium* : Topological insulators. *Rev. Mod. Phys.* **82**, 3045–3067 (2010).

[6] X.-L. Qi, S.-C. Zhang, Topological insulators and superconductors. *Rev. Mod. Phys.* **83**, 1057–1110 (2011).

[7] X.-L. Qi, T. L. Hughes, S.-C. Zhang, Topological field theory of time-reversal invariant insulators. *Phys. Rev. B* **78**, 195424 (2008).

[8] A. M. Essin, J. E. Moore, D. Vanderbilt, Magnetoelectric polarizability and axion electrodynamics in crystalline insulators. *Phys. Rev. Lett.* **102**, 146805 (2009).

[9] C.-Z. Chang, *et al.*, Zero-field dissipationless chiral edge transport and the nature of dissipation in the quantum anomalous hall state. *Phys. Rev. Lett.* **115**, 057206 (2015).

[10] Y. H. Wang, *et al.*, Observation of chiral currents at the magnetic domain boundary of a topological insulator. *Science* **349**, 948-952 (2015).

[11] M. C. Rechtsman, *et al.*, Topological creation and destruction of edge states in photonic graphene. *Phys. Rev. Lett.* **111**, 103901 (2013).

[12] Y. Plotnik, *et al.*, Observation of unconventional edge states in photonic graphene. *Nat. Mater.* **13**, 57-62 (2014). Article.

[13] Z. Wang, Y. D. Chong, J. D. Joannopoulos, M. Soljačić, Reflection-free one-way edge modes in a gyromagnetic photonic crystal. *Phys. Rev. Lett.* **100**, 013905 (2008).

[14] Z. Wang, Y. Chong, J. D. Joannopoulos, M. Soljacic, Observation of unidirectional backscattering-immune topological electromagnetic states. *Nature (London)* **461**, 772-U20 (2009).

[15] M. Hafezi, E. A. Demler, M. D. Lukin, J. M. Taylor, Robust optical delay lines with topological protection. *Nat. Phys.* **7**, 907-912 (2011).

[16] K. Fang, Z. Yu, S. Fan, Realizing effective magnetic field for photons by controlling the phase of dynamic modulation. *Nat. Photon.* **6**, 782-787 (2012).

[17] A. B. Khanikaev, *et al.*, Photonic topological insulators. *Nat. Mater.* **12**, 233-239 (2013).

[18] L. Lu, J. D. Joannopoulos, M. Soljaclc, Topological photonics. *Nat. Photon.* **8**, 821-829 (2014).

[19] X. Huang, Y. Lai, Z. H. Hang, H. Zheng, C. T. Chan, Dirac cones induced by accidental

degeneracy in photonic crystals and zero-refractive-index materials. *Nat. Mater* **10**, 582-586 (2011).

[20] J. Mei, Y. Wu, C. T. Chan, Z.-Q. Zhang, First-principles study of Dirac and Dirac-like cones in phononic and photonic crystals. *Phys. Rev. B* **86**, 035141 (2012).

[21] P. Moitra, *et al.*, Realization of an all-dielectric zero-index optical metamaterial. *Nat. Photon.* **7**, 791-795 (2013).

[22] Y. Li, *et al.*, On-chip zero-index metamaterials. *Nat. Photon.* **9**, 738-742 (2015).

[23] A. Fang, Z. Q. Zhang, S. G. Louie, C. T. Chan, Klein tunneling and supercollimation of pseudospin-1 electromagnetic waves. *Phys. Rev. B* **93**, 035422 (2016).

[24] D. Guzmán-Silva, *et al.*, Experimental observation of bulk and edge transport in photonic Lieb lattices. *New J. Phys.* **16**, 063061 (2014).

[25] S. Mukherjee, *et al.*, Observation of a localized flat-band state in a photonic Lieb lattice. *Phys. Rev. Lett.* **114**, 245504 (2015).

[26] R. A. Vicencio, *et al.*, Observation of localized states in Lieb photonic lattices. *Phys. Rev. Lett.* **114**, 245503 (2015).

[27] F. Diebel, D. Leykam, S. Kroesen, C. Denz, A. S. Desyatnikov, Conical diffraction and composite Lieb bosons in photonic lattices. *Phys. Rev. Lett.* **116**, 183902 (2016).

[28] S. Taie, *et al.*, Coherent driving and freezing of bosonic matter wave in an optical Lieb lattice. *Sci. Adv.* **1** (2015).

[29] M. Rizzi, V. Cataudella, R. Fazio, Phase diagram of the Bose-Hubbard model with $\sqcup_3$ symmetry. *Phys. Rev. B* **73**, 144511 (2006).

[30] A. A. Burkov, E. Demler, Vortex-peierls states in optical lattices. *Phys. Rev. Lett.* **96**, 180406 (2006).

[31] D. Bercioux, D. F. Urban, H. Grabert, W. Häusler, Massless Dirac-Weyl fermions in a T_3 optical lattice. *Phys. Rev. A* **80**, 063603 (2009).

[32] B. Dóra, J. Kailasvuori, R. Moessner, Lattice generalization of the Dirac equation to general spin and the role of the flat band. *Phys. Rev. B* **84**, 195422 (2011).

[33] A. Raoux, M. Morigi, J.-N. Fuchs, F. Piéchon, G. Montambaux, From dia- to paramagnetic orbital susceptibility of massless fermions. *Phys. Rev. Lett.* **112**, 026402 (2014).

[34] T. Andrijauskas, *et al.*, Three-level Haldane-like model on a dice optical lattice. *Phys. Rev. A* **92**, 033617 (2015).

[35] F. Wang, Y. Ran, Nearly flat band with Chern number $c = 2$ on the dice lattice. *Phys. Rev. B* **84**, 241103 (2011).

[36] J. Wang, H. Huang, W. Duan, Z. Liu, Identifying Dirac cones in carbon allotropes with square symmetry. *The Journal of Chemical Physics* **139** (2013).

[37] W. Li, M. Guo, G. Zhang, Y.-W. Zhang, Gapless MoS_2 allotrope possessing both massless Dirac and heavy fermions. *Phys. Rev. B* **89**, 205402 (2014).

[38] J. Romhanyi, K. Penc, R. Ganesh, Hall effect of triplons in a dimerized quantum magnet. *Nat. Commun* **6** (2015). Article.

[39] G. Giovannetti, M. Capone, J. van den Brink, C. Ortix, Kekulé textures, pseudospin-one Dirac cones, and quadratic band crossings in a graphene-hexagonal indium chalcogenide bilayer. *Phys. Rev. B* **91**, 121417 (2015).

[40] R. Shen, L. B. Shao, B. Wang, D. Y. Xing, Single Dirac cone with a flat band touching on line-centered-square optical lattices. *Phys. Rev. B* **81**, 041410 (2010).

[41] D. F. Urban, D. Bercioux, M. Wimmer, W. Häusler, Barrier transmission of Dirac-like pseudospin-one particles. *Phys. Rev. B* **84**, 115136 (2011).

[42] M. Vigh, *et al.*, Diverging dc conductivity due to a flat band in a disordered system of pseudospin-1 Dirac-Weyl fermions. *Phys. Rev. B* **88**, 161413 (2013).

[43] J. T. Chalker, T. S. Pickles, P. Shukla, Anderson localization in tight-binding models with flat bands. *Phys. Rev. B* **82**, 104209 (2010).

[44] J. D. Bodyfelt, D. Leykam, C. Danieli, X. Yu, S. Flach, Flatbands under correlated perturbations. *Phys. Rev. Lett.* **113**, 236403 (2014).

[45] E. H. Lieb, Two theorems on the Hubbard model. *Phys. Rev. Lett.* **62**, 1201–1204 (1989).

[46] H. Tasaki, Ferromagnetism in the Hubbard models with degenerate single-electron ground states. *Phys. Rev. Lett.* **69**, 1608–1611 (1992).

[47] H. Aoki, M. Ando, H. Matsumura, Hofstadter butterflies for flat bands. *Phys. Rev. B* **54**, R17296–R17299 (1996).

[48] C. Weeks, M. Franz, Topological insulators on the Lieb and perovskite lattices. *Phys. Rev. B* **82**, 085310 (2010).

[49] N. Goldman, D. F. Urban, D. Bercioux, Topological phases for fermionic cold atoms on the Lieb lattice. *Phys. Rev. A* **83**, 063601 (2011).

[50] J. Vidal, R. Mosseri, B. Douçot, Aharonov-Bohm cages in two-dimensional structures. *Phys. Rev. Lett.* **81**, 5888–5891 (1998).

[51] D. S. Novikov, Elastic scattering theory and transport in graphene. *Phys. Rev. B* **76**, 245435 (2007).

[52] M. I. Katsnelson, F. Guinea, A. K. Geim, Scattering of electrons in graphene by clusters of impurities. *Phys. Rev. B* **79**, 195426 (2009).

[53] J.-S. Wu, M. M. Fogler, Scattering of two-dimensional massless Dirac electrons by a circular potential barrier. *Phys. Rev. B* **90**, 235402 (2014).

[54] J. Cserti, A. Pályi, C. Péterfalvi, Caustics due to a negative refractive index in circular graphene *p-n* junctions. *Phys. Rev. Lett.* **99**, 246801 (2007).

[55] R. L. Heinisch, F. X. Bronold, H. Fehske, Mie scattering analog in graphene: Lensing, particle confinement, and depletion of Klein tunneling. *Phys. Rev. B* **87**, 155409 (2013).

[56] M. M. Asmar, S. E. Ulloa, Rashba spin-orbit interaction and birefringent electron optics in graphene. *Phys. Rev. B* **87**, 075420 (2013).

[57] B. Liao, M. Zebarjadi, K. Esfarjani, G. Chen, Isotropic and energy-selective electron cloaks on graphene. *Phys. Rev. B* **88**, 155432 (2013).

[58] M. M. Asmar, S. E. Ulloa, Spin-orbit interaction and isotropic electronic transport in graphene. *Phys. Rev. Lett.* **112**, 136602 (2014).

[59] A. Ferreira, T. G. Rappoport, M. A. Cazalilla, A. H. Castro Neto, Extrinsic spin hall effect induced by resonant skew scattering in graphene. *Phys. Rev. Lett.* **112**, 066601 (2014).

[60] Y. Zhao, *et al.*, Creating and probing electron whispering-gallery modes in graphene. *Science* **348**, 672–675 (2015).

[61] W. S. Bakr, J. I. Gillen, A. Peng, S. Folling, M. Greiner, A quantum gas microscope for detecting single atoms in a Hubbard-regime optical lattice. *Nature* **462**, 74-77 (2009).

[62] D. Jin, *et al.*, Topological magnetoplasmon. *arXiv:1602.00553* (2016).

ACKNOWLEDGEMENTS

This work was supported by ONR under Grant No. N00014-16-1-2828.